Geometric Mechanics of Curved Crease Origami

Marcelo A. Dias,[1,*] Levi H. Dudte,[2,†] L. Mahadevan,[3,‡] and Christian D. Santangelo[1,§]

[1]*Department of Physics, University of Massachusetts Amherst, Amherst, Massachusetts 01002, USA*
[2]*Engineering and Applied Sciences, Harvard University, Cambridge, Massachusetts 02138, USA*
[3]*Physics and Engineering and Applied Sciences, Harvard University, Cambridge, Massachusetts 02138, USA*

(Received 4 June 2012; revised manuscript received 16 August 2012; published 13 September 2012)

Folding a sheet of paper along a curve can lead to structures seen in decorative art and utilitarian packing boxes. Here we present a theory for the simplest such structure: an annular circular strip that is folded along a central circular curve to form a three-dimensional buckled structure driven by geometrical frustration. We quantify this shape in terms of the radius of the circle, the dihedral angle of the fold, and the mechanical properties of the sheet of paper and the fold itself. When the sheet is isometrically deformed everywhere except along the fold itself, stiff folds result in creases with constant curvature and oscillatory torsion. However, relatively softer folds inherit the broken symmetry of the buckled shape with oscillatory curvature and torsion. Our asymptotic analysis of the isometrically deformed state is corroborated by numerical simulations that allow us to generalize our analysis to study structures with multiple curved creases.

DOI: 10.1103/PhysRevLett.109.114301 PACS numbers: 46.70.−p, 46.32.+x, 62.20.mq

Over the last few decades, origami has evolved from an art form into a scientific discipline, where folding techniques have been widely applied to fields of engineering, architecture, and design [1–4], made possible in large part by methods for the mathematical analysis of folded surfaces. Although there are artistic and technological precedents for folding paper along curves [5–10], as seen in Japanese paper boxes and the ubiquitous box for fries, how these geometrical structures get their physical shape is poorly understood, so that the potential associated with curve folding for constructing (quasi)isometric structures using real materials and corrugated shells [11,12] is still only poorly tapped. In this Letter, we consider the geometry and mechanics of the simplest case of a curved fold: an annular elastic sheet folded along a closed, circular curve that buckles out of the plane to resolve a fundamental incompatibility between the folded geometry and the ensuing mechanical stresses.

Qualitative experiments with a complete circular annulus of paper having a concentric, circular crease show that folding buckles the crease into a saddle [Fig. 1(a)], while the same crease along a cut annulus remains planar [Fig. 1(b)]. This behavior is a consequence of a fundamental incompatibility between the geometry of the fold and the stretching elasticity of the sheet. As we will see, and as apparent in Fig. 1(b), the sheet responds to folding by wrapping around itself to eliminate in-plane mechanical stresses. The closed annulus, on the other hand, can relax these stresses by buckling. In the limit of the sheet where the thickness is much smaller than the width, which is itself smaller than the length of the crease, the shape that arises is a balance between the bending energy of the sheets on either side of the crease, the energy at the crease itself, and the geometrical constraints arising from the sheet's closed topology, similar to that seen in the mechanics of strips [13], shells [14], and non-Euclidean objects [15].

We consider an annulus of uniform thickness $t$and width $2w$ folded along a central circular crease of radius r ($t \ll w < r$). In the deformed state, the crease is a space curve parametrized by arc length s, with curvature $\kappa(s)$ and torsion $\tau(s)$, and the surfaces on either side of it come together at a finite fold (or dihedral) angle $\theta(s)$. Assuming isometric deformations away from the crease, the midsurface of the sheet on either side of the crease is developable. Then any point on it can be characterized in terms of a set of

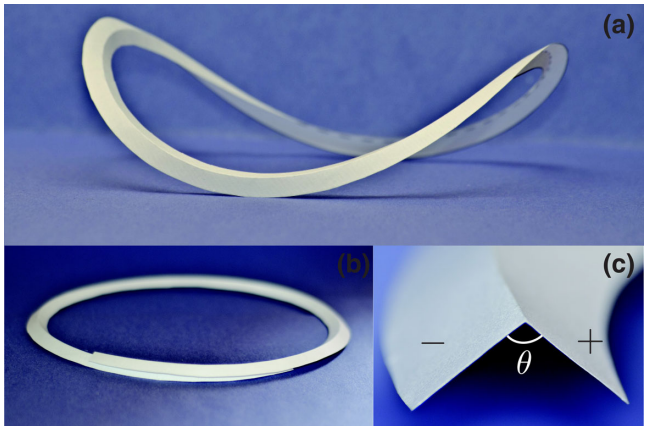

FIG. 1 (color online). A photograph of the model built by cutting a flat annulus of width $2w$ from a flat sheet of paper with central circle of radius r. (a) Folding along its center line buckles the structure out of plane. However, if we cut the annulus, (b), the structure collapses to an overlapping planar state, with curvature given by Eq. (1). (c) The inset shows a cross section of the fold, where the right and the left planes, $\mathbf{X}_+$ and $\mathbf{X}_-$, define the dihedral angle θ.

coordinates (s, v), corresponding to the arc length and the generators of the developable surface on the inside and outside of the crease, $\mathbf{g}_\pm$ [see Fig. 1(c)], with the coordinates $\mathbf{X}_\pm(s, v) = \mathbf{X}(s, 0) + v\mathbf{g}_\pm(s)$. For developable surfaces, the generators must also satisfy the condition that $\mathbf{g}_\pm(s) \times d\mathbf{g}_\pm(s)/ds$ is perpendicular to the crease [16]. Since folding does not induce in-plane strains, the projection of the crease curvature onto the tangent plane on either side of the sheet must remain $1/r$. This leads to two geometrical conditions [8] that relate the dihedral angle of the crease to its spatial curvature and the angle of the generators of the developable surface on either side of it. They read

$$\sin\left(\frac{\theta}{2}\right) = \frac{1}{\kappa}, \tag{1}$$

$$\cot\gamma_\pm = -\frac{1}{2}\left(2\tau \pm r\frac{d\theta}{ds}\right)\tan\left(\frac{\theta}{2}\right), \tag{2}$$

where κ/r and τ/r are the curvature and torsion of the crease, respectively, and $\gamma_\pm$ is the angle between the unit tangent vector of the crease $d\mathbf{X}(s)/ds$ and the generator. We see that $\kappa(s) \geq 1$, with equality only when $\theta = \pi$. For a circular crease concentric with a circular annulus of constant dimensionless half-width $\omega = w/r$, we find

$$v_\pm^{\max}(\xi) = \pm\sin\gamma_\pm(\xi) \mp \sqrt{\omega^2 \mp 2\omega + \sin^2\gamma_\pm(\xi)} \tag{3}$$

to be the dimensionless distance to the boundary along a generator leaving the crease from a point labeled by the dimensionless arc length $\xi = s/r$.

The energy of the sheet is the sum of the energy of deforming the sheet on either side of the crease and that of the fold that connects them. Since the creased folded surface is piecewise developable, the energy per unit surface is proportional to the square of the mean curvature [17]. The mean curvature on either side of the sheet is

$$H_\pm(\xi, v) = \frac{\pm\cot(\theta/2)\csc\gamma_\pm}{2r[\sin\gamma_\pm \mp v(1 \pm \gamma'_\pm)]}, \tag{4}$$

where $(.)' = d/d\xi(.)$. Then the energy of each surface $E_b = B\int_0^{2\pi}\int_0^{v_\pm^{\max}} H_\pm^2 dv d\xi$, where B is the bending stiffness of the material of the sheet. Carrying out the integral along the generators, v, explicitly leads to the following scaled bending energy for the two surfaces:

$$\frac{E_b}{B} = \frac{1}{8}\int_0^{2\pi} d\xi \sum_\pm \frac{\cot^2(\theta/2)\csc^2\gamma_\pm}{1 \pm \gamma'_\pm} \times \ln\left[\frac{\sin\gamma_\pm}{\sin\gamma_\pm - v_\pm^{\max}(\xi)(1 \pm \gamma'_\pm)}\right]. \tag{5}$$

We see that Eq. (5) is determined entirely in terms of the geometry of the crease. To model the fold itself, we use a phenomenological energy functional measuring the deviation of $\theta(\xi)$ from an equilibrium angle θ_0, which we assume to be constant, so that the scaled crease energy is as follows:

$$\frac{E_c}{B} = \frac{\varsigma}{2}\int_0^{2\pi} d\xi\left[\cos\left(\frac{\theta(\xi)}{2}\right) - \cos\left(\frac{\theta_0}{2}\right)\right]^2, \tag{6}$$

where $\varsigma = Kr/B$ is the ratio of the crease stiffness K and the bending stiffness B. This energy reduces to a simple quadratic expression in the difference $\theta - \theta_0$ when $\theta \sim \theta_0$; although the precise form of this term does not affect our analytic results, it conforms to our numerical model [18].

The equilibrium shape of the curved crease results from minimizing $E = E_b + E_c$ and is characterized by three parameters: the scaled natural width of the ribbon ω, the natural dihedral angle between the two surfaces adjoining the crease θ_0 and the dimensionless crease-surface energy scale ς, subject to appropriate boundary conditions. For example, an open circular crease has free ends and thus prefers to remain planar with $\tau = 0$, since nonplanarity would increase both the curvature and torsion (see Supplemental Material [19]). A closed crease, however, is frustrated by geometry, forcing it to buckle, a fact that follows from the inequality $\kappa = 1/\sin(\theta/2) > 1$ when $\theta < \pi$, which requires $\int d\xi\kappa > 2\pi$, and is incompatible with a planar crease with $\tau = 0$ [8].

Although geometrical constraints induce buckling, the resulting fold shapes are determined by minimizing the total elastic energy consisting of contributions from the sheet [Eq. (5)] and the fold [Eq. (6)], expressed entirely in terms of the curvature and torsion of the crease [13,20]. For relatively narrow but stiff folds, i.e., $\omega \ll 1$ and $\varsigma \gg 1$ are weakly folded, the dihedral angle $\theta_0 \sim \pi$, and hence $\epsilon \equiv 1/\sin(\theta_0/2) - 1 \ll 1$. Then, we find that the total scaled energy $E = (E_b + E_c)/B$ simplifies to (see Supplemental Material [19])

$$E \approx \int_0^{2\pi} d\xi\left\{\frac{\varsigma}{4\epsilon}\left(\kappa - 1 - \epsilon\right)^2 + \frac{\omega}{2}\tau^2\right\} \tag{7}$$

in terms of the scaled curvature κ and torsion τ. We see that as $\varsigma \to \infty$, the rescaled curvature $\kappa \to 1/\sin(\theta_0/2) = 1 + \epsilon$, the prescribed curvature. The minimal energy crease shape, therefore, minimizes τ^2 subject to the constraints of fixed length and curvature. In this limit, the Euler-Lagrange equations become $[\tau'' + (1 + \epsilon)^2\tau]' \approx 0$ at constant curvature (see Supplemental Material [19]). If $\epsilon = 0$, corresponding to a dihedral angle $\theta_0 = \pi$, the solution to these equations is infinitely smooth. Otherwise, a solution of continuity class C^4 may be obtained to these equations with $\kappa = 1 + \epsilon$ and oscillating torsion

$$\delta\tau = \begin{cases} \tau_0\left[1 - \frac{\cos[(\xi - \pi/2)(1+\epsilon)]}{\cos[(\pi/2)(1+\epsilon)]}\right], & 0 \leq \xi \leq \pi \\ -\tau_0\left[1 - \frac{\cos[(\xi - 3\pi/2)(1+\epsilon)]}{\cos[(\pi/2)(1+\epsilon)]}\right], & \pi \leq \xi \leq 2\pi. \end{cases} \tag{8}$$

The absolute magnitude of the torsion τ_0 is then determined by the condition that the curved fold has an arc length $2\pi r$, and consistent with the four-vertex theorem for closed

convex space curves, there are four points with vanishing torsion [21].

To go further, we can carry out an asymptotic analysis of the Euler-Lagrange equations obtained by minimizing $E = E_b + E_c$; this must be performed by expanding the shape of the crease around a planar curve of constant curvature, κ_0. Following Refs. [13,20], we write $\kappa = \kappa_0 + \delta\kappa$ and $\tau = \delta\tau$ and compute the Euler-Lagrange equations. To lowest order, we obtain an algebraic expression determining the ideal curvature of the crease κ_0 for arbitrary ς, ϵ, and ω (see Supplemental Material [19]), the curvature of an incomplete or severed planar annular fold with zero torsion. To next order, we find that both the curvature and torsion oscillate; a typical analytical solution is shown in Fig. 2(a), with the inset showing the oscillating torsion vanishing at the extrema of the curvature (see Fig. 1). Here, the overall amplitude of τ is chosen to close

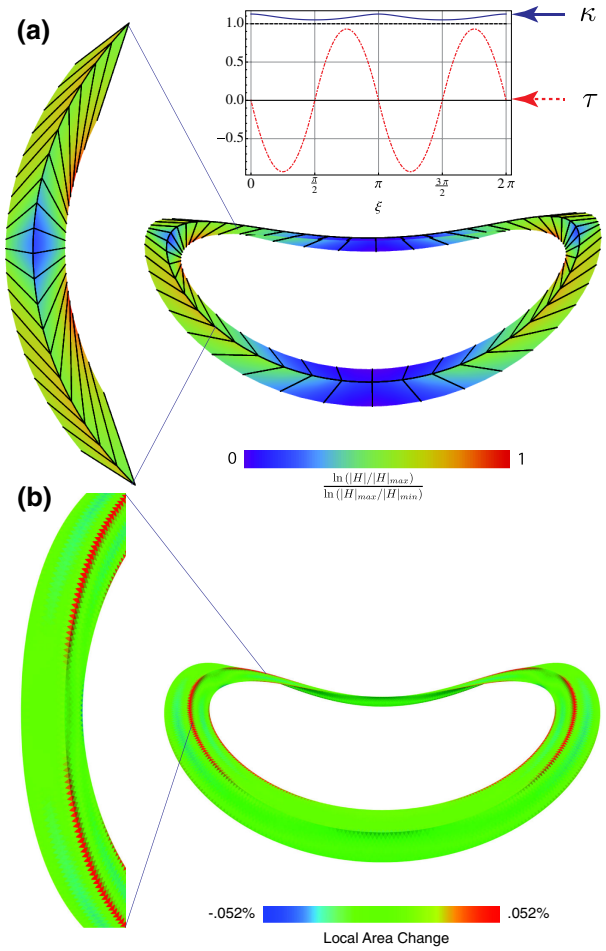

FIG. 2 (color online). (a) Perturbative fold of width $\omega = 0.1$ and $\varsigma = 2/\sqrt{3}$ shaded by mean curvature. The generators are indicated by the lines on the surface. The inset shows the dimensionless torsion and curvature of the crease. (b) A simulated fold of width $\omega \approx .0994$ shaded by local area change relative to the flat state.

the curve, with $\theta(0)$ and $\theta(\pi/2)$ parametrizing the solutions (see Supplemental Material [19]).

These qualitative features are also confirmed by direct numerical minimization of the energy of a triangular mesh model for the curved origami structure, in which each edge is treated as a linear spring, with the stretching stiffness inversely proportional to rest length. We apply restorative bending forces to the adjacent triangles in each sheet so that they prefer collinear normals, with the scaled ratio of the bending stiffness to the stretching stiffness $B/Sl^2 \approx 10^{-6}$. Adjacent triangles that straddle the crease prefer a fixed, nonplanar dihedral angle [18] (see SI). The presence of a small but finite extensibility of this model implies that our simulations relax the isometry of the folding process and thus allow us to capture how the extension and shear arise in wide folds [Fig. 2(b)]. We find that the extensional and shear strains typically localize where the mean curvature becomes large, consistent with our isometric analytic theory [shown in Fig. 2(a)].

Moving beyond the simple asymptotic theory for narrow folds, we consider the dependence of the solution on the scaled width by using the perturbative shapes as a variational ansatz in the exact expression for the energy $E_b + E_c$. Since the shapes have a fourfold symmetry, we expect to see a coincidence between $\theta(0)$ and $\theta(\pi/2)$. In Fig. 3(a), we plot $|\theta(0) - \theta(\pi/2)|$ for the minimal energy configuration as a function of the scaled width ω. We see that when $\omega \lesssim 0.1$, annuli with large ς have a nearly constant dihedral angle around the entire length of the fold, with $\theta(0) \approx \theta(\pi/2)$ for the narrowest fold widths. However, for small ς, the energy minimum generically has $\theta(0) \neq \theta(\pi/2)$; this discrepancy increases with the scaled width ω. Plotting the corresponding energy landscape in Figs. 3(b)–3(d) for some representative values of ω, we see that the energy contours develop forks, because the range of $\theta(0)$ and $\theta(\pi/2)$ are forbidden by the geometric constraints that the generators of our two surfaces can intersect only outside the actual surface, else the bending energy diverges.

To avoid the intersection of generators inside the outer surface, it is required that

$$\gamma'_+ < \frac{\sin\gamma_+}{v_+^{\max}} - 1 \quad \text{and} \quad \gamma'_- > -\frac{\sin\gamma_-}{v_-^{\max}} + 1, \tag{9}$$

which expression reduces to $|\tau'| < (1-\omega)\cot(\theta/2)/\omega$ at the points where $\tau = 0$. Similarly, to avoid the intersection of the generators on the inner surface inside the inner boundary requires the discriminant in Eq. (3) to be positive, implying a bound on the torsion,

$$\left|\tau + \frac{\theta'}{2}\right| < \frac{1-\omega}{\sqrt{2\omega - \omega^2}} \cot\left(\frac{\theta}{2}\right). \tag{10}$$

These geometrical bounds restrict the range of allowed torsion and thus the buckling of the crease. As a consequence, wide folds will become resistant to deformations as the sheet quickly reaches a regime where the generators

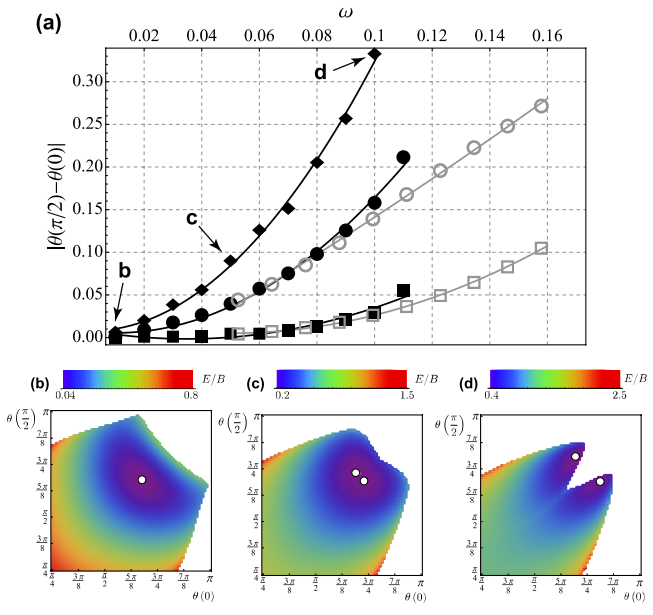

FIG. 3 (color online). (a) Angle differences $|\theta(\pi/2) - \theta(0)|$ as a function of ω with $\theta_0 = 2\pi/3$. The curve with diamonds are computed from the first-order perturbation theory with $\varsigma = 2/\sqrt{3}$ and $\theta_0 = 2\pi/3$. The numerical simulations are shown in gray with $\varsigma = 2\sqrt{3}$ (open circles) and $\varsigma = 160/\sqrt{3}$ (open squares), and are compared with nonperturbative variational ansatz, $\kappa_{(2)}$ and $\tau_{(2)}$, described in the text with $\varsigma = \sqrt{3}/40$ (circles) and $\varsigma = \sqrt{3}/2$ (squares). Corresponding energy landscapes, as a function of $\theta(0)$ and $\theta(\pi/2)$, respectively, are shown for (b) $\omega = 0.01$, (c) 0.05, and (d) 0.1, with energy minima drawn as white dots.

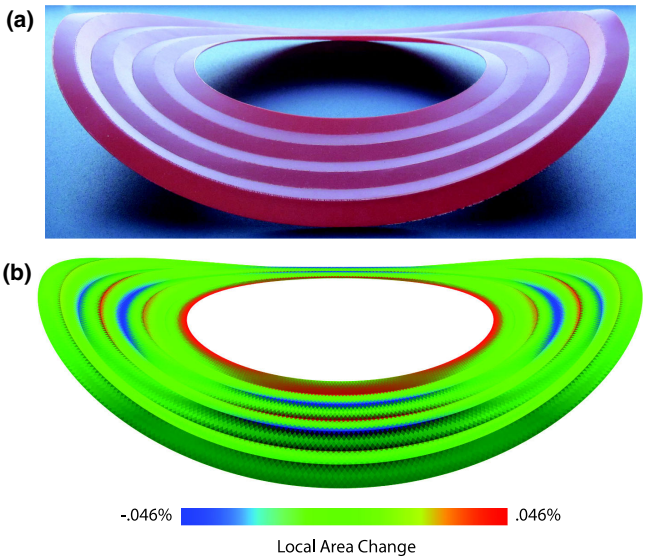

FIG. 4 (color online). (a) A plastic model of six circular folds generated by perforating the folds at equal intervals with a laser cutter. The ratio of outer to inner boundary is 2. (b) A simulation result with the same planar geometry as the plastic model shaded by local area change. Multiple fold simulation has the same magnitude order of area change as that of single fold simulation and agrees visually with the physical model in (a).

start to nearly intersect in the neighborhood of $\xi = \pi/2$. In Fig. 3(d), this is manifested by the presence of large forks carved out by the forbidden configurations. Since energy minima occur close to the singularities, our perturbative expansion of the shape is approximate at best. However, even at intermediate widths, where the perturbative expansion should be at least qualitatively valid, bifurcation of the minima show up in the shadows of the prominent forks observed in Fig. 3(d).

These calculations suggest a second improved ansatz: $\kappa_{(2)} = \kappa_0 + \kappa_1 \cos(2\xi)$ and $\tau_{(2)} = \tau_0[\sin(2\xi) + \eta \sin(4\xi)]$, choosing τ_0 to close the fold and η to minimize the energy. When $\eta = 0$, we now find very good agreement with the perturbative ansatz previously considered. However, we find that $\eta \approx -0.45$ for large widths, which lowers the maximum of the torsion and better satisfies the singularity bounds in Eqs. (9) and (10). Using ς as a fitting parameter, we see that $\theta(\pi/2) - \theta(0)$ agrees quite well with the numerical solutions for small ω and only diverges from numerical simulations for large widths around $\omega \sim 0.08$, as shown in Fig. 3(a).

Finally, we consider structures built from multiple, concentric folds (Fig. 4). Again, the large penalty for stretching leads to strong geometric constraints connecting the curvature and torsion of the crease to the dihedral angle of the fold given by Eq. (1), leading to self-similar creases and folds. The generator on the outside of a crease must coincide with the generator on the inside of the next crease, fixing the angle γ_+ on the inside of the next crease, while the torsion determines the relationship between γ_+ and γ_-, so that the direction of the next set of generators emerges. This procedure follows from the first crease to the last crease, until we reach a boundary or the generators cross. Our numerical simulations confirm this and further show that multiple creases stretch very little and do buckle rigidly.

Our study of curved crease origami shows that a consequence of the fundamental frustration between folding along a curve and the avoidance of singularities and in-plane stretching imposes geometric constraints on the shape that are reflected in a bifurcation of the curvature of a closed crease of large width. Indeed, the coupling between shape and in-plane stretching endows these structures with a stiffness and response that is unusual, as we have demonstrated in the simplest of situations—a closed circular fold. Moving forward, our approach may be generalized to more complex curves having variable dihedral angles in folded structures with curved creases, and thus sets the stage for the analysis and design of these objects.

We thank Tom Hull and Pedro Reis for discussions, Badel Mbanga for help with photography, and NSF DMR 0846582, the NSF-supported MRSEC on Polymers at UMass (DMR-0820506) (M. D., C. S.), the Wyss Institute for Bioinspired Engineering (L. D., L. M.), and the MacArthur Foundation (L. M.) for support.

*madias@physics.umass.edu
†ldudte@seas.harvard.edu
‡lm@seas.harvard.edu
§csantang@physics.umass.edu

[1] K. Miura, in *Method of Packing and Deployment of Large Membranes in Space* (The Institute of Space and Astronautical Science, 1980).
[2] E. Demaine and P. ORourke, *Geometric Folding Algorithms* (Cambridge University, Cambridge, England, 2009).
[3] E. Hawkes, B. An, N. M. Benbernou, H. Tanaka, S. Kim, E. D. Demaine, D. Rus, and R. J. Wood, Proc. Natl. Acad. Sci. U.S.A. **107**, 12441 (2010).
[4] M. Schenk and S. D. Guest, in *Origami Folding: A Structural Engineering Approach, Origami 5*, edited by Mark Yim (A K Peters Ltd, Wellesley, MA, 2011).
[5] H. M. Wingler, *Bauhaus: Weimar, Dessau, Berlin, Chicago* (MIT, Cambridge, MA, 1969).
[6] D. A. Huffman, IEEE Trans. Comput. **C-25**, 1010 (1976).
[7] J. P. Duncan and J. L. Duncan, Proc. R. Soc. A **383**, 191 (1982).
[8] D. Fuchs and S. Tabachnikov, Am. Math. Mon. **106**, 27 (1999).
[9] H. Pottmann and J. Wallner, *Computational Line Geometry* (Springer-Verlag, Berlin, 2001).
[10] M. Kilian, S. Flöry, Z. Chen, N. J. Mitra, A. Sheffer, and H. Pottmann, ACM Trans. Graph. **27**, 1 (2008).
[11] J. P. Duncan, J. L. Duncan, R. Sowerby, and B. S. Levy, Sheet Metal Industries **58**, 527 (1981).
[12] K. A. Seffen, Phil. Trans. R. Soc. A **370**, 2010 (2012).
[13] E. L. Starostin and G. H. M. van der Heijden, Phys. Rev. E **79**, 066602 (2009).
[14] B. Audoly and Y. Pomeau, *Elasticity and Geometry: From Hair Curls to the Nonlinear Response of Shells* (Oxford University, New York, 2010).
[15] C. D. Santangelo, Europhys. Lett. **86**, 34003 (2009).
[16] M. P. do Carmo, *Differential Geometry of Curves and Surfaces* (Prentice-Hall, Englewood Cliffs, NJ, 1976).
[17] A. E. H. Love, *A Treatise on the Mathematical Theory of Elasticity* (Dover, New York, 1944).
[18] R. Bridson, S. Marino, and R. Fedkiw, *ACM SIGGRAPH/ Eurographics Symposium on Computer Animation (SCA), 2003*, pp. 28–32.
[19] See Supplemental Material at http://link.aps.org/supplemental/10.1103/PhysRevLett.109.114301 for a derivation of the fold energy and analytical perturbation theory.
[20] R. Capovilla, C. Chryssomalakos, and J. Guven, J. Phys. A **35**, 6571 (2002).
[21] V. D. Sedykh, Bull. Lond. Math. Soc. **26**, 177 (1994).

Geometric Mechanics of Curved Crease Origami: Supplementary Information

Marcelo A. Dias,[1] Levi H. Dudte,[2] L. Mahadevan,[3] and Christian D. Santangelo[1]

[1]*Department of Physics, University of Massachusetts Amherst, Amherst, Massachusetts 01002*
[2]*Engineering and Applied Sciences, Harvard University, Cambridge, Massachusetts 02138*
[3]*Physics and Engineering and Applied Sciences, Harvard University, Cambridge, Massachusetts 02138*

(Dated: August 14, 2012)

I. THE ELASTIC ENERGY

We model paper folding in two steps: (i) A crease is imposed, which we model as having geodesic curvature $1/r$, and (ii) the sheet away from the crease is deformed isometrically. The process of creasing is not simple, and is ultimately represented by the phenomenological energy, equation (6). Since the mid-surface of the paper away from the crease is a developable, the energy arises entirely from bending and takes the form $E_b = B\int_0^{2\pi}\int_{\pm}^{v_{\pm}^{max}} H_{\pm}^2 dv d\xi$.

A developable has the form $\mathbf{X}_{\pm}(s,v) = \mathbf{X}(s,0)+v\mathbf{g}_{\pm}(s)$, from which we can compute the mean curvature everywhere in (s,v) coordinates as

$$H_{\pm}(s,v) = \frac{\kappa_{N\pm}(s)\csc\gamma_{\pm}(s)/2}{\sin\gamma_{\pm}(s) \mp v(\kappa_g(s) \pm \gamma'_{\pm}(s))}, \tag{SI-1}$$

where we use the variables of the Darboux frame [1]: geodesic curvature, normal curvature, and geodesic torsion. These are given by $\kappa_g = 1/r = \kappa(s)\sin[\theta(s)/2]$, $\kappa_{N\pm}(s) = \pm\kappa(s)\cos[\theta(s)/2]$, and $\tau_{g\pm}(s) = \tau(s) \pm \theta'(s)/2$ respectively. The generator angle is represented by $\tan[\gamma_{\pm}(s)] = \mp\kappa_{N\pm}(s)/\tau_{g\pm}(s)$. Therefore, the total bending energy may be integrated along the generator,

$$E_b = \frac{B}{8}\int_0^L ds \sum_{\pm} \frac{\kappa_{N\pm}^2 \csc^2\gamma_{\pm}}{\kappa_g \pm \gamma'_{\pm}} \ln\left(\frac{\sin\gamma_{\pm}}{\sin\gamma_{\pm} - w_{\pm}\left(\kappa_g \pm \gamma'_{\pm}\right)}\right). \tag{SI-2}$$

If we specialize in curves with constant curvature and a finite constant width w on either side of the crease, simple geometry yields an expression for the distance to the boundary *along the generators*,

$$\kappa_g w_{\pm} = \pm\sin\gamma_{\pm} \mp \sqrt{\kappa_g^2 w^2 \mp 2\kappa_g w + \sin^2\gamma_{\pm}}. \tag{SI-3}$$

The radicand in this expression must be positive, yielding a lower bound on $\gamma_{\pm}$. When this bound is violated, a generator no longer reaches the inner boundary; instead it must contact the crease again further downstream, leading to another type of singularity.

When the crease is a straight line, $\kappa_g = 0$, Equation (SI-2) simplifies to

$$E_b = \frac{B}{2}\int_0^L ds \frac{\kappa^2\left(1+(\tau/\kappa)^2\right)^2}{w\,(\tau/\kappa)'} \ln\left(\frac{1+w\,(\tau/\kappa)'}{1-w\,(\tau/\kappa)'}\right), \tag{SI-4}$$

the energy for a straight developable strip of width w [2, 3]. Alternatively, a narrow strip arises from the limit $w_{\pm} \approx w/\sin\gamma_{\pm} \to 0$ in equation (SI-2). Expanding in powers of the surface width w, we obtain

$$E_b \;\approx\; \frac{Bw}{8}\int_0^L ds\left[\kappa_{N+}(s)^2\csc^4\gamma_+(s) + \kappa_{N-}(s)^2\csc^4\gamma_-(s)\right]. \tag{SI-5}$$

Rewriting equation (SI-5) in terms of the geometric quantities in the Darboux frame, we obtain

$$E_b \;\approx\; \frac{Bw}{8}\int_0^L ds\left[\kappa_N^{(+)2}(s)\left(1+\frac{\tau_g^{(+)2}(s)}{\kappa_N^{(+)2}(s)}\right)^2 + \kappa_N^{(-)2}(s)\left(1+\frac{\tau_g^{(-)2}(s)}{\kappa_N^{(-)2}(s)}\right)^2\right]. \tag{SI-6}$$

This result recapitulates Sadowsky's functional for an infinitesimal strip when $\kappa_g = 0$ [4].

II. ENERGY AND EULER-LAGRANGE EQUATIONS FOR SMALL WIDTHS AND TORSION

We substitute $\kappa_N^{(\pm)} = \pm\sqrt{\kappa^2 - r^{-2}}$ and $\tau_g^{(\pm)} = \tau \pm \theta'/2$ in Eq. (SI-6). In terms of dimensionless curvature κ/κ_g, torsion τ/κ_g and arc length $\xi = \kappa_g s$, we obtain the bending energy

$$E_b \approx \frac{B\omega}{8}\int_0^{2\pi} d\xi \left[\left(\kappa^2-1\right)\left(1+\frac{\left(\tau+\theta'/2\right)^2}{\left(\kappa^2-1\right)}\right)^2 + \left(\kappa^2-1\right)\left(1+\frac{\left(\tau-\theta'/2\right)^2}{\left(\kappa^2-1\right)}\right)^2\right], \tag{SI-7}$$

where $\omega = \kappa_g w$ and $(\cdot)'$ indicates a derivative with respect to ξ.

As described in the text, we supplement Eq. (SI-7) with a crease energy

$$E_c = \frac{\varsigma B}{2}\int_0^{2\pi} d\xi \ \left[\cos\left(\theta/2\right) - \cos\left(\theta_0/2\right)\right]^2, \tag{SI-8}$$

with a prescribed angle θ_0. When $\epsilon \equiv \sin(\theta_0/2) - 1 \ll 1$, *i.e.* the crease is almost flat, and the crease stiffness $\varsigma \ll 1$ is large, we expect $\tau \ll 1$ and $\theta' \ll 1$. Expanding Eq. (SI-7) in quadratic order, we obtain

$$E_b \approx \frac{B\omega}{8}\int_0^{2\pi} d\xi \left(\kappa^2 - 1 + 4\tau^2 + \theta'^2\right). \tag{SI-9}$$

For large ς, we expand the curvature κ around its prescribed value $1/\sin(\theta_0/2) = 1+\epsilon$, and obtain

$$\frac{E_c + E_b}{B} \approx \int_0^{2\pi} d\xi \ \left\{\frac{\varsigma}{4\epsilon}\left(\kappa - 1 - \epsilon\right)^2 + \frac{\omega}{2}\tau^2\right\}. \tag{SI-10}$$

To minimize Eq. (SI-10), we find the first variation of $E = E_b + E_c$ with respect to the shape of the crease, $\mathbf{X}(s)$. Since we have already assumed that the torsion is small and ς is large so that κ is close to its prescribed value, we will derive this variation to *linear* order in τ. To this end, we note that

$$\delta\kappa = \frac{1}{\kappa}\mathbf{X}''\cdot(\delta\mathbf{X})'', \tag{SI-11}$$

and, after a long calculation,

$$\int ds\ \tau\delta\tau \approx \int ds\ \left[-\left(\frac{\tau\kappa'}{\kappa^2}\right)'' - (\tau\kappa)' - \left(\frac{\tau}{\kappa}\right)'''\right]\hat{\mathbf{b}}\cdot\delta\mathbf{X}, \tag{SI-12}$$

where $\hat{\mathbf{b}}$ is the unit binormal to the curve, defined as $\hat{\mathbf{b}} = (\partial_s\mathbf{X}\times\partial_s^2\mathbf{X})/\kappa$. This variation also requires that we introduce a Lagrange multiplier to constrain s to be the arc length of the crease, *i.e.* $\partial_s\mathbf{X}^2 = 1$. Finally, this yields the Euler-Lagrange equations

$$0 \approx \left[\frac{\kappa'' - \kappa^2\left(\kappa - 1 - \epsilon\right)}{\kappa}\right]' + 2\kappa\kappa' + \left(\kappa - 1 - \epsilon\right)\kappa' \tag{SI-13}$$

$$0 \approx -w\left[\left(\frac{\tau}{\kappa}\right)''' + (\tau\kappa)' + \left(\frac{\tau\kappa'}{\kappa^2}\right)''\right] + \frac{\varsigma}{2\epsilon}\left[2\kappa'\tau + \left(\kappa - 1 - \epsilon\right)\tau'\right].$$

The first of these equations clearly has a solution when $\kappa = 1+\epsilon$, and in fact this it the value preferred by the energy as $\varsigma \to \infty$. Using $\kappa = 1+\epsilon$ in the second equation, one obtains an equation for the torsion

$$\tau''' + (1+\epsilon)^2\tau' = 0. \tag{SI-14}$$

Thus, the torsion can vary even for constant curvature; this variation is necessary in order to keep the arc length independent of the crease.

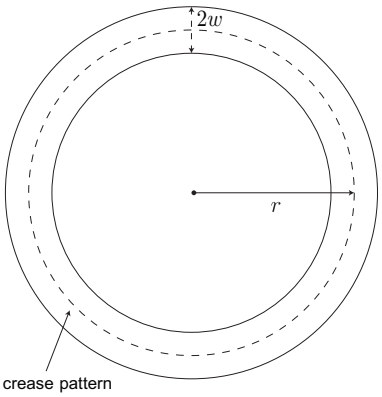

FIG. SI-1: The crease pattern of the prototype model. The parameters of the problem, width w and radius of curvature r of the crease, are indicated.

III. *ANSATZ* FOR SHAPE FROM PERTURBATION THEORY

In this section, we discuss details of the perturbative calculation used to construct an *ansatz* for the shape of the crease. We start with a circular crease of radius r between two concentric, circular boundaries with radii $r - w$ and $r + w$ (being $w/r \sim 0.1$), as shown in FIG. SI-1. The preferred angle is set by E_c to be θ_0. The geometrical constraint between the dihedral angle of the fold and curvature of the crease allows us to associate a curvature $(1 + \epsilon)/r$ with this angle, where

$$\sin\left(\frac{\theta_0}{2}\right) = \frac{1}{1+\epsilon}. \tag{SI-15}$$

Since $\epsilon > 0$, the preferred curvature of the crease is always larger than $1/r$; as discussed in the text, this requires us to accommodate this additional curvature by buckling the crease out of the plane.

The generator angles with respect to the tangent, $\gamma_\pm$ can be expressed in terms of the dimensionless curvature, torsion, and the rate of change of the dihedral angle of the fold with respect to $\xi = s/r$ as follows [5, 6],

$$\cot\gamma_\pm(s) = -\frac{[\tau(s) \pm \theta'(s)/2]}{\cot[\theta(s)/2]}. \tag{SI-16}$$

equation (SI-16) provides the relationships,

$$\tau(s) = -\cot\left[\frac{\theta(s)}{2}\right]\frac{\sin[\gamma_+(s)+\gamma_-(s)]}{\sin\gamma_+(s)\sin\gamma_-(s)} \tag{SI-17}$$

and

$$\theta'(s) = -\cot\left[\frac{\theta(s)}{2}\right]\frac{\sin[\gamma_+(s)-\gamma_-(s)]}{2\sin\gamma_+(s)\sin\gamma_-(s)}. \tag{SI-18}$$

We can write an expansion of the curvatures and torsions around a planar state,

$$\begin{aligned}\kappa(s) &= \kappa_0 + \delta\kappa(s) + \mathcal{O}(\delta\kappa^2) \\ \tau(s) &= \delta\tau(s) + \mathcal{O}(\delta\tau^2),\end{aligned} \tag{SI-19}$$

and solve the Euler-Lagrange equations for the fold order-by-order.

To zeroth order, we obtain the relationship between κ_0 and the control parameters ς, ϵ and $\omega = w/r$,

$$\varsigma = \frac{\kappa_0^2(1+\epsilon)\left(1+\kappa_0^2\right)\ln(1-\omega)/4}{2\left(\kappa_0^2-2\right)\kappa_0\sqrt{\frac{2\epsilon+\epsilon^2}{\kappa_0^2-1}} + (1+\epsilon)\left(3-2\kappa_0^2\right) + \kappa_0^2/(1+\epsilon)}. \tag{SI-20}$$

The parameter κ_0 is the curvature of lowest energy that would be achieved on an incomplete, and therefore torsionless, fold. Fig. SI-2 shows the solutions for κ_0 as a function of ς and dimensionless width ω for different values of ϵ. For

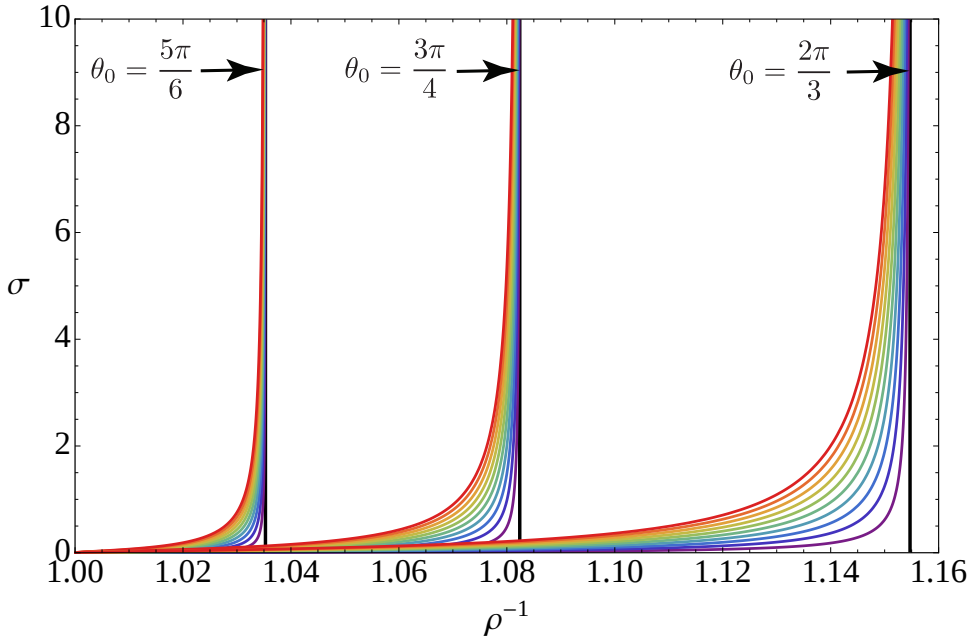

FIG. SI-2: Zeroth order solution. Dependence ς as a function of the solutions for the zeroth-order curvature, κ_0. The vertical lines represent three different preferred angles set in the phenomenological energy, $\theta_0 = \{2\pi/3, 3\pi/4, 5\pi/6\}$. The color scheme from red to purple represent the normalized widths, $\omega \equiv w/r$, from 0.02 to 0.2

large ς ($1/\varsigma \lesssim 0.1$), κ_0 approaches the preferred curvature $1+\epsilon$ as expected. We can find an approximate solution, valid when ς is large, by expanding in powers of $1/\kappa_0 - 1/(1+\epsilon)$ to obtain

$$\kappa_0 \approx 1 + \epsilon + \frac{\epsilon(1+\epsilon)(2+\epsilon)[2+\epsilon(2+\epsilon)]\ln(1-\omega)}{8\varsigma}. \tag{SI-21}$$

To first order, the Euler-Lagrange equations give us coupled equations for $\delta\kappa(s)$ and $\delta\tau(s)$,

$$\begin{aligned} A_0\delta\kappa + A_2\partial_s^2\delta\kappa + A_4\partial_s^4\delta\kappa + A_6\partial_s^6\delta\kappa + B_1\partial_s\delta\tau + B_3\partial_s^3\delta\tau &= 0 \\ \bar{A}_2\partial_s^2\delta\kappa + \bar{A}_4\partial_s^4\delta\kappa + \bar{B}_1\partial_s\delta\tau + \bar{B}_3\partial_s^3\delta\tau + \bar{B}_5\partial_s^5\delta\tau &= 0, \end{aligned} \tag{SI-22}$$

with constant coefficients,

$$
\begin{aligned}
A_0 &\equiv -\varsigma\left(\frac{3}{\kappa_0^2}-\frac{2\sqrt{2\epsilon+\epsilon^2}\kappa_0^3}{(1+\epsilon)(\kappa_0^2-1)^{3/2}}-\frac{1}{(1+\epsilon)^2}+2\right)-\frac{\left(1+3\kappa_0^2\right)\ln(1-\omega)}{4}\\
A_2 &\equiv -\frac{2\varsigma}{\kappa_0^4(1+\epsilon)}\left[3(1+\epsilon)-\left(\frac{1}{\kappa_0^2-1}+3\right)\kappa_0\sqrt{\frac{2\epsilon+\epsilon^2}{\kappa_0^2-1}}\right]\\
&\quad -\frac{\omega^3\left(1+4\kappa_0^2\right)-2\omega\left(1+2\kappa_0^2\right)+2(\omega-1)^2(\omega+1)\left(2-3\kappa_0^2\right)\ln(1-\omega)}{4(\omega-1)^2(\omega+1)\left(1-\kappa_0^2\right)}\\
A_4 &\equiv -\frac{1}{\kappa_0^2(\kappa_0^2-1)}\frac{\omega^3\left(1+7\kappa_0^2\right)+\omega^2\kappa_0^2-2\omega\left(1+3\kappa_0^2\right)+2(\omega+1)(\omega-1)^2\left(1-3\kappa_0^2\right)\ln(1-\omega)}{4(\omega-1)^2(\omega+1)}\\
A_6 &\equiv \frac{(2-3\omega)\omega+2(\omega-1)^2\ln(1-\omega)}{4(\omega-1)^2\kappa_0^2(\kappa_0^2-1)}\\
B_1 &\equiv \frac{\omega^2\kappa_0}{4(\omega-1)^2(\omega+1)\sqrt{\kappa_0^2-1}}\\
B_3 &\equiv \frac{B_1}{\kappa_0^2}=\frac{\omega^2}{4(\omega-1)^2(\omega+1)\kappa_0\sqrt{\kappa_0^2-1}}\\
\bar{A}_2 &\equiv \frac{\omega^2}{4(\omega-1)^2(\omega+1)\sqrt{\kappa_0^2-1}}\\
\bar{A}_4 &\equiv \frac{\bar{A}_2}{\kappa_0^2}=\frac{\omega^2}{4(\omega-1)^2(\omega+1)\kappa_0^2\sqrt{\kappa_0^2-1}}\\
\bar{B}_1 &\equiv \kappa_0\frac{\omega\left(\omega^2-2\right)}{4(\omega-1)^2(\omega+1)}-\frac{2\varsigma}{\kappa_0^3}\left(\kappa_0\frac{\sqrt{2\epsilon+\epsilon^2}}{\sqrt{\kappa_0^2-1}(1+\epsilon)}-1\right)\\
\bar{B}_3 &\equiv \frac{1}{\kappa_0}\frac{\omega^3\left(1+3\kappa_0^2\right)+\omega^2\kappa_0^2-2\omega\left(1+\kappa_0^2\right)+2(\omega+1)(\omega-1)^2\left(1-\kappa_0^2\right)\ln(1-\omega)}{4(\omega-1)^2(\omega+1)}\\
\bar{B}_5 &\equiv \frac{1}{4\kappa_0}\left[\frac{\omega(3\omega-2)}{(\omega-1)^2}-2\ln(1-\omega)\right],
\end{aligned}
\tag{SI-23}
$$

Since Eqs. (SI-22) are linear, they can be solved with a linear superposition of complex exponentials,

$$
\begin{aligned}
\delta\kappa &= \sum_{n=1}^{11} C_n e^{k_n\xi}\\
\delta\tau &= \sum_{n=1}^{11} \bar{C}_n e^{k_n\xi}.
\end{aligned}
\tag{SI-24}
$$

for some set of complex wave numbers k_n which must be determined numerically, and coefficients C_n and $\bar{C}_n$. Thus, we search for oscillating curvature and torsion solutions. Based on the observed shapes and a four-vertex theorem for convex space curves [7], we expect four points of vanishing torsion. Thus, we decompose a single closed fold into four segments of dimensionless length $\pi/2$ with vanishing torsion at their endpoints and choose boundary conditions such that the four pieces can be reassembled into a closed shape. From Eq. (SI-17), points of vanishing torsion will have $\gamma_+(\xi)+\gamma_-(\xi)=\pi$ while Eq. (SI-18) implies that points of extremal angle, at which $\theta'=0$, have $\gamma_+=\gamma_-$. In Eqs. (refeq:odes1), the number of derivatives of torsion is odd while those of curvature is even. Thus, we expect that the points of vanishing torsion coincide with those of extremal curvature and, therefore, $\gamma_+(s)=\gamma_-(s)=\pi/2$ so that the generators are aligned and perpendicular to the curve at these points. These assumptions are consistent with observations of simulated and paper closed folds.

In principle, we can set additional boundary conditions for τ' at both ends of the simulated pieces. As a practical matter, the solutions to Eqs. (SI-22) have several extremely small length scales, k_n^{-1} owing to the small size of $A_6\propto\omega^3$ and $\bar{B}_5\propto\omega^3$. This makes determining the solution from boundary conditions numerically stiff. Assuming that the shape of the torsion is of sufficiently long length scale, we neglect the highest order derivatives in Eqs. (SI-22) in determining our solution. Thus, we are able to set τ' at one end of a piece of fold. By setting the overall scale

of the oscillating torsion, this results in a solution shape that is in continuity class C^4. Nevertheless, this small non-analyticity does not cause any change in the computation of the energy.

To summarize, we set $\theta' = \tau = 0$ at $\xi = 0$, $\pi/2$, π, and $3\pi/2$, and set $\theta(\pi) = \theta(0)$ and $\theta(\pi/2) = \theta(3\pi/2)$. Finally, the perturbative solution is expressible in terms of three parameters only, $\theta(0)$, $\theta(\pi/2)$ and $\tau'(0)$. Finally, we set $\tau'(0)$ by requesting that the fold, resulting from gluing all four pieces together, is closed. This can be imposed by integration of the Frenet-Serret system under periodic boundary conditions,

$$\frac{d}{ds}\begin{pmatrix}\hat{\mathbf{t}}\\ \hat{\mathbf{n}}\\ \hat{\mathbf{b}}\end{pmatrix} = \begin{pmatrix}0 & \kappa & 0\\ -\kappa & 0 & \tau\\ 0 & -\tau & 0\end{pmatrix}\begin{pmatrix}\hat{\mathbf{t}}\\ \hat{\mathbf{n}}\\ \hat{\mathbf{b}}\end{pmatrix}, \tag{SI-25}$$

where the triad of vectors $\{\hat{\mathbf{t}}, \hat{\mathbf{n}}, \hat{\mathbf{b}}\}$ represents the moving tangent, normal, and binormal on the curve. Therefore, the moduli space consistent with closed origami is a manifold defined by $\delta\tau'(0) = \delta\tau'|_{\xi=0}[\theta(0), \theta(\pi/2)]$. In order to explore the landscape of energy for the allowed configurations, we substitute the solutions for (SI-22) and (SI-23) into the total energy density and integrate it over the domain $\xi \in [0, 2\pi]$. The result gives the total energy as a function of the two remaining parameters, $\theta(0)$ and $\theta(\pi/2)$, $E = E[\theta(0), \theta(\pi/2)]$.

IV. NUMERICAL MODEL

Our numerical model was created by using triangulated meshes to represent the initial, planar setup of the curved origami. These meshes are essentially hexagonal grids, designed such that each internal angle $\pi/3$. The mesh used in Fig. 2b has 7,650 nodes and 14,400 faces, with an effective width of .0994. The mesh shown in Fig. 4b has 15,050 nodes and 29,040 faces and an outer radius twice that of its inner radius with six uniformly spaced folds.

We endow these triangulated meshes with elastic stretching and bending modes to capture the in-plane and out-of-plane deformation of thin sheets. The stretching mode simply treats each edge in the mesh as a linear spring, all edges having the same stretching stiffness. Accordingly, the magnitude of the restorative elastic forces applied to each node in a deformed edge with rest length x_0 and stretching stiffness k is given by $\frac{k_s}{x_0}(x' - x_0)$ and the energy contained in a deformed edge is given by $\frac{k_s}{2x_0}(x' - x_0)^2$. The x_0 term in denominator of the stretching mode ensures mesh-independence. The bending mode is characterized in terms of four vectors u_1, u_2, u_3 and u_4, each of which is applied to a node in a pair of adjacent triangles. Defining the weighted normal vectors $N_1 = (x_1 - x_3) \times (x_1 - x_4)$ and $N_2 = (x_2 - x_4) \times (x_2 - x_3)$ and the shared edge $E = x_4 - x_3$, we may write

$$u_1 = |E|\frac{N_1}{|N_1|^2} \tag{SI-26}$$

$$u_2 = |E|\frac{N_2}{|N_2|^2} \tag{SI-27}$$

$$u_3 = \frac{(x_1 - x_4)\cdot E}{|E|}\frac{N_1}{|N_1|^2} + \frac{(x_2 - x_4)\cdot E}{|E|}\frac{N_2}{|N_2|^2} \tag{SI-28}$$

$$u_4 = -\frac{(x_1 - x_3)\cdot E}{|E|}\frac{N_1}{|N_1|^2} - \frac{(x_2 - x_2)\cdot E}{|E|}\frac{N_2}{|N_2|^2}. \tag{SI-29}$$

The relative magnitudes of these vectors constitute a pure geometric bending mode for a pair of adjacent triangles. For pairs of adjacent triangles that *do not* straddle the fold line, the force on each vertex is given by

$$F_i = k_b\frac{|E|^2}{|N_1| + |N_2|}\sin(\theta/2)u_i \tag{SI-30}$$

where k_b is the mesh-independent bending stiffness and $\sin(\theta/2) = \pm\sqrt{1 - \hat{n_1}\cdot\hat{n_2}/2}$ is the dihedral angle function that makes each u_i equivalent to an elastic restorative force. The normalization scales the magnitude of F_i to ensure that k_b is mesh-independent. For pairs of adjacent triangles that *do* straddle the fold line, the $\sin(\theta/2)$ term is shifted by the rest angle θ_0 so that the force on each vertex is given by

$$F_i = k_b\frac{|E|^2}{|N_1| + |N_2|}(\sin(\theta/2) - \sin(\theta_0/2))u_i. \tag{SI-31}$$

This shift makes the rest configuration of a pair of adjacent triangles non-planar and provides the mechanism by which we simulate the local plasticity of a fold. Just as a piece of folded paper retains its fold rather than returning to its initial planar state, the adjacent triangles that straddle the curved fold line in the simulated mesh bend out of the plane toward their rest angles. The bending energy contained in a pair of adjacent triangles is given by

$$E_b = \frac{k_b}{2} \int_{\theta_0}^{\theta} (\sin \frac{\theta}{2} - \sin \frac{\theta_0}{2}) \mathrm{d}\theta \tag{SI-32}$$

where k_b is the bending stiffness (*** we need to be precise about the form of the energy here - so how does the pre factor appear ? ***) and $\frac{|E|^2}{|N_1|+|N_2|}$, which is quadratic in $\theta - \theta_0$ for $\theta \sim \theta_0$, in agreement with the phenomenological energy form in the analytical model.

We introduce viscous damping so that the simulation eventually comes to rest. Damping forces are computed at every vertex with different coefficients for each oscillatory mode, bending and stretching. We distinguish between these two modes by projecting the velocities of the vertices in an adjacency onto the bending mode, and the velocities of the vertices in an edge onto the stretching mode.

The discrete model enables us to construct an equation of motion for each vertex to describe the dynamic behavior of the mesh. This equation takes the form

$$\ddot{x} = \frac{1}{m} f(x, \dot{x}) \tag{SI-33}$$

where x is the position of the vertex in world coordinates, m is the vertex mass and $f(x, \dot{x})$ is the incident force vector function on the vertex in terms of its position vector x and velocity vector $\dot{x}$. We discretize this equation and use the Velocity Verlet numerical integration method to update the positions and velocities of the vertices. At any time $t + \Delta t$ during the simulation we can approximate the position $x(t + \Delta t)$ and the velocity $\dot{x}(t + \Delta t)$ of a vertex as

$$x(t + \Delta t) = x(t) + \dot{x}(t)\, \Delta t + \frac{1}{2} \ddot{x}(t)\, \Delta t^2 \tag{SI-34}$$

$$\dot{x}(t + \Delta t) = \dot{x}(t) + \frac{\ddot{x}(t) + \ddot{x}(t + \Delta t)}{2}\, \Delta t \tag{SI-35}$$

A single position, velocity and accleration update then follows a simple algorithm.

- Compute $x(t + \Delta t)$
- Compute $\ddot{x}(t + \Delta t)$ using $x(t + \Delta t)$ for stretching and bending forces and $\dot{x}(t)$ for damping forces
- Compute $\dot{x}(t + \Delta t)$

Note that this algorithm staggers the effects of damping on the simulation by Δt.

The physical model shown in Fig. 4a was cut from a thin plastic sheet using a laser cutter. The folds were created by laser cutting fine perforated lines, and the model was then folded by hand. Its geometry matches that of the simulation shown in Fig. 4b, where we started with a planar annulus and used the natural angle of each curved fold (assumed to be identical) as a single fitting parameter.

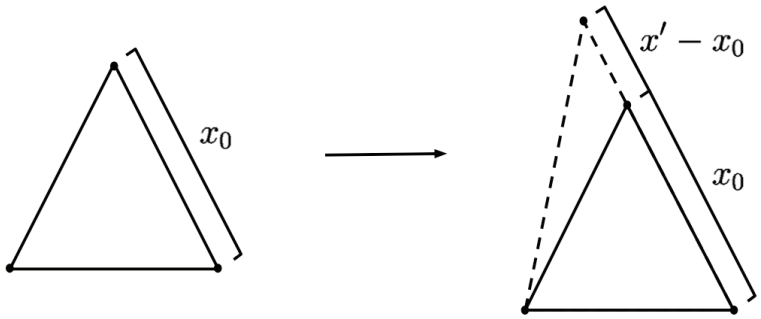

FIG. SI-3:

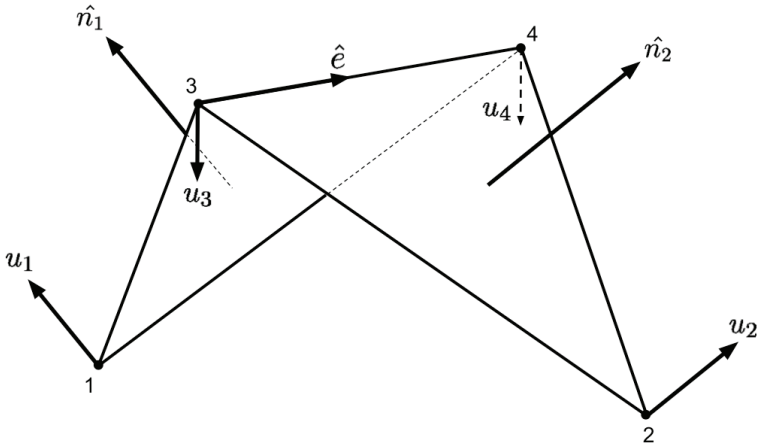

FIG. SI-4:

[1] M. P. do Carmo, *Differential Geometry of Curves and Surfaces* (Prentice-Hall, Englewood Cliffs, 1976).
[2] W Wunderlich, Monatsh. Math **66**, 276 (1962).
[3] E. L. Starostin and G. H. M. van der Heijden, Nature Materials **6**, 563 - 567 (2007).
[4] M. Sadowsky, Sitzungsber. Preuss. Akad. Wiss. **22**, 412-415 (1930).
[5] D. Fuchs and S. Tabachnikov, The American Mathematical Monthly **106**, No. 1, 27-35 (1999).
[6] J. P. Duncan and J. L. Duncan, Proceedings of the Royal Society of London. Series A, Mathematical and Physical Sciences **383**, No. 1784, 191-205 (1982).
[7] V. D. Sedykh, Bull. London Math. Soc. **26**, 2, 177-180 (1994).